REPORTS OF PRACTICAL ONCOLOGY AND RADIOTHERAPY 24 (2019) 606–613

Available online at www.sciencedirect.com

ScienceDirect

journal homepage: http://www.elsevier.com/locate/rpor

Original research article

Evaluating the accuracy of geometrical distortion correction of magnetic resonance images for use in intracranial brain tumor radiotherapy

Seyed Mehdi Bagherimofidi[a], *Claus Chunli Yang*[b], *Roberto Rey-Dios*[c], *Madhava R. Kanakamedala*[b], *Ali Fatemi*[b,d,*]

[a] *Department of Biomedical Engineering, Aliabad Katoul Branch, Islamic Azad University, Aliabad Katoul, Iran*
[b] *Department of Radiation Oncology, University of Mississippi Medical Center, Jackson, MS 39216, United States*
[c] *Department of Neurosurgery, University of Mississippi Medical Center, Jackson, MS 39216, United States*
[d] *Department of Radiology, University of Mississippi Medical Center, Jackson, MS 39216, United States*

ARTICLE INFO

Article history:
Received 18 March 2019
Received in revised form
14 June 2019
Accepted 21 September 2019
Available online 19 October 2019

Keywords:
MRI guided radiotherapy
MRI image geometric distortion correction
Radiotherapy
Magnetic resonance imaging
Intracranial brain tumor radiotherapy

ABSTRACT

Aim: Determine the 1) effectiveness of correction for gradient-non-linearity and susceptibility effects on both QUASAR GRID^{3D} and CIRS phantoms; and 2) the magnitude and location of regions of residual distortion before and after correction.

Background: Using magnetic resonance imaging (MRI) as a primary dataset for radiotherapy planning requires correction for geometrical distortion and non-uniform intensity.

Materials and Methods: **Phantom Study:** MRI, computed tomography (CT) and cone beam CT images of QUASAR GRID^{3D} and CIRS head phantoms were acquired. **Patient Study:** Ten patients were MRI-scanned for stereotactic radiosurgery treatment. **Correction algorithm:** Two magnitude and one phase difference image were acquired to create a field map. A MATLAB program was used to calculate geometrical distortion in the frequency encoding direction, and 3D interpolation was applied to resize it to match 3D T1-weighted magnetization-prepared rapid gradient-echo (MPRAGE) images. MPRAGE images were warped according to the interpolated field map in the frequency encoding direction. The corrected and uncorrected MRI images were fused, deformable registered, and a difference distortion map generated.

Results: Maximum deviation improvements: **GRID**^{3D}, 0.27 mm y-direction, 0.07 mm z-direction, 0.23 mm x-direction. **CIRS**, 0.34 mm, 0.1 mm and 0.09 mm at 20-, 40- and 60-mm diameters from the isocenter. Patient data show corrections from 0.2 to 1.2 mm, based on location. The most-distorted areas are around air cavities, e.g. sinuses.

Conclusions: The phantom data show the validity of our fast distortion correction algorithm. Patient-specific data are acquired in <2 min and analyzed and available for planning in less than a minute.

Published by Elsevier B.V. on behalf of Greater Poland Cancer Centre.

* Corresponding author at: Department of Radiation Oncology and Radiology, University of Mississippi Medical Center, 2500 North State Street Jackson, Mississippi 39216, United States.
E-mail address: afatemi@umc.edu (A. Fatemi).
https://doi.org/10.1016/j.rpor.2019.09.011
1507-1367/Published by Elsevier B.V. on behalf of Greater Poland Cancer Centre.

1. Introduction

The use of magnetic resonance imaging (MRI) images as the sole modality for radiotherapy (RT) treatment planning requires geometrically corrected MRI images with uniform signal intensity.[1,2] In modern scanners, the signal intensity in a given voxel has been corrected using special filtering, such as pre-scan normalization and hardware optimization using multi-array radio frequency (RF) coils.[3] However, the quantification and correction accuracy for geometrical distortion is more problematic, and much more critical, since it is systematic and sequence dependent. The magnitude of the images' geometrical distortion depends on the MRI machine brand, magnetic field strength, gradient type as well as the type of MRI pulse sequences and parameters used for patient scanning.[4,5] Experimental data shows the minimal distortion at the center of a closed bore magnet and increasing gradually toward the radial edges of the scanning volume.[4] The maximum distortion can be greater than 3 mm, even for head scans with a small field of view.[6] Recently, it has been shown that even small distortions of less than 1.3 mm in MRI images used for RT planning may result in significant under-dose (up to 30%) of specific very small targets.[7]

In general radiotherapy practice, radiation is planned to cover the target tumor meanwhile sparing surrounding normal tissue or organs at risk (OAR) of radiation damage. This process associated with some uncertainties originated from tumor delineation, patient setup, and inter/intra-fractional target/organ movement which are corrected for by adding margins to the tumor and normal tissues.[8] Many centers use MRI images co-registered with computed tomography (CT) images, but because of uncertainty in co-registration and overall time-consuming clinical flow, MRI-only RT planning is a favorite practice.[9] In either approach, the best and most precise target delineation with no or minimal geometrical distortion is sought during stereotactic radiosurgery (SRS) treatment planning.

The recent decades have witnessed a substantial progress in tumor diagnosis, staging and radiation delivery. The gross target volumes (GTV) have evolved from two-dimensional to highly conformal three- and four-dimensional definition.[6] Still, though, this process is performed by clinicians and so is highly dependent on the accuracy of primary planning images and may be prone to geometrical distortion, which is very common in MRI images.[10] With the increasing accuracy and complexity of RT delivery, it is necessary to assess this error and be certain about the location of GTVs and their extent.[11,12]

We have found it essential to study the geometrical distortion of MRI images when they are used as a primary RT planning dataset. Such study will also help to assess potential improvements that new techniques or techniques like anatomical and functional MRI or Positron Emission Tomography (PET) can bring to target volume definition.[13,14]

However, there is no documented tolerance in geometrical uncertainty. Since the effect of geometrical distortion on RT dose delivery depends on many parameters, such as the target volume, location, prescription dose, dose gradient and the desired conformity, it is generally acknowledged that RT planning requires images with high geometrical accuracy and precision.[1,9] Thus, there is a need to develop and evaluate customized MRI pulse sequences and correction algorithm for RT treatment planning with minimum geometrical distortion, specially for highly conformal plans with multiple beams and targets located at the periphery of the brain or near the sinuses and cavities.[15]

The present work focuses on the assessment of our new MRI geometrical distortion correction algorithm using commercially available solutions and a few patients. We introduce the clinical flow which can be implemented in any radiation oncology setup access to MRI scanner. We measured the MRI geometrical distortion on phantoms before and after correction and use patient data to show the variability of distortion magnitude based on location and head shape. Our goals are to determine 1) the effectiveness of correction for gradient-nonlinearity and susceptibility effect on both QUASAR GRID^{3D} and CIRS phantoms; 2) the magnitude and location of regions of residual distortion before and after correction.

2. Material and methods

A 1.5 T Siemens MAGNETOM Aera RT edition MRI machine (Siemens Healthcare, Erlangen, Germany) was commissioned based on an established quality control procedure for RT treatment planning.[16] Using commercially available phantoms and healthy volunteers, we optimized MRI pulse sequences for clinical relevance, signal-to-noise ratio (SNR), and ability to provide artifact-free images with high signal uniformity. We used a 32-channel RF multiarray head coil with a regular diagnostic table top. For phantom studies, we used a head-size MRI-compatible quality assurance (QA) phantom (Fig. 1; Quasar GRID^{3D}, Modus Medical, London, Ontario, Canada) and a CIRS MRI distortion phantom for SRS QA (Fig. 1; MRI Distortion Phantom for SRS, Model 603A, CIRS, Norfolk, Virginia, USA).

Both phantoms were MRI-scanned using a Toshiba Aquilion one CT-Simulator (Toshiba Medical Systems Corporation, Otawara, Tochigi, Japan), and cone beam CT (CBCT) images with a 2 mm slice thickness were acquired using an XVI Elekta Synergy (Elekta Ltd, Crawley, UK) machine. These images were used to evaluate geometrical stability. For both the phantom and patient study, the main MRI pulse sequence for geometrical evaluation was a 3D T1-weighted magnetization-prepared rapid gradient-echo (MPRAGE), $1 \times 1 \times 1\,mm^3$, time of repetition (TR)/ time of echo (TE) = 2200/2.91 ms, flip angle = 15°, receiver bandwidth = 300 Hz/pixel. All scans were run with both 3D geometrical distortion correction and pre-scan normalization filters on. We previously measured the B_0 inhomogeneity and gradient non-linearity using a QUASAR MRI^{3D} Modus medical MRI RT QA phantom (Fig. 2) to correct for machine-related geometrical distortion.

The inhomogeneity of magnetic field changes the position of pixels in the frequency encoding direction. The field map contains the phase change of spins because of main field imperfection (B_0) and magnetic susceptibility of the patient or phantom. If x is the frequency encoding direction, the distortion in this direction is equal to ref.[17]:

$$\Delta x\,[mm] = \Delta B / G_{fe} \rightarrow \Delta x\,[px] = \Delta\varphi / (2\pi BW)$$

Fig. 1 – GRID ^{3D} MRI phantom (A) and CIRS SRS MRI QA head phantom (B).

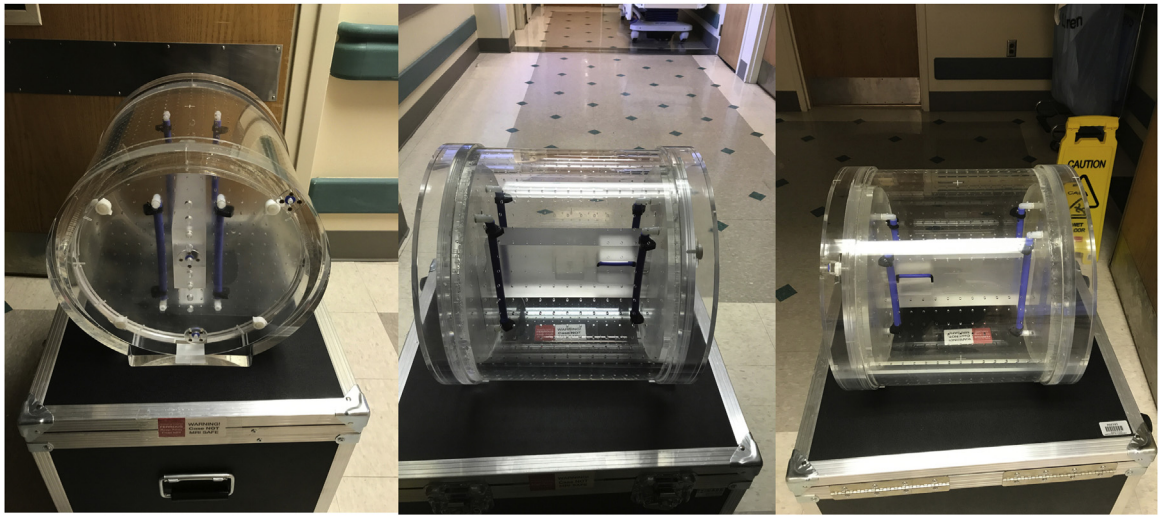

Fig. 2 – Modus MRI^{3D} MRI phantom.

in which ΔB is the magnetic field inhomogeneity, G_{fe} is gradient in the frequency direction, $\Delta\varphi$ is the field map in $\left[\frac{rad}{s}\right]$, and BW is the bandwidth in $\left[\frac{Hz}{px}\right]$. The right side is the distortion in mm, and the left side is its counterpart, in pixels (px). The spatial mispositioning was altered in the frequency encoding direction using the distortion map:

$$x_{distorted} = x_{correct} + \Delta x$$

To create the distortion map, the field map acquired using a modified fast multi-echo gradient echo (mGRE) sequence with $TE_1 = 9.52$ ms and $TE_2 = 4.76$ ms was used to calculate the complex phase difference map with receiver bandwidth and isotropic resolution, close to T1W-MPRAGE. Two magnitude and one phase difference images were collected; then, the field map in radians was created in FMRIB Software Library v 6.0 (FSL; Analysis Group, Oxford, UK) (Fig. 3). MATLAB 9.1 (The MathWorks Inc., Natick, MA) code created by our group was used to calculate the geometric distortion in the frequency encoding direction (Fig. 3). In the program, the MPRAGE and the field map pixels were mapped to the same reference coordinate of the table. 3D interpolation was applied to calculate the geometric distortion map for each pixel of MPRAGE image, creating a "correction map". The MPRAGE image was warped according to the correction map in the frequency encoding direction.

For the phantom study, both GRID^{3D} and CIRS MRI images (T1-MPRAGE) were corrected and compared with uncorrected MRI images acquired using just the vendor software. In the patient study, ten patients were MRI-scanned for SRS treatment. After MRI image correction, MimVista v. 6.8 (MIM Software Inc., Cleveland, OH, USA) was used to fuse corrected and non-corrected MRI images, deformable registered, and generate the difference distortion map (Fig. 4).

3. Results

For the GRID^{3D} phantom we looked at maximum and minimum deviations, and minimum absolute deviation ± standard deviation before and after correction (Table 1). We noted maximum improvements in geometrical distortion of 0.27 mm in

Table 1 – Geometrical distortion error (in mm) for 3D GRID^{3D} phantom before and after applying our geometrical distortion correction algorithm. We analyzed the results for three different planes (axial, sagittal and coronal), 3D images, three coordinates (Dx, Dy and Dz), and Dr (the distance from MRI machine isocenter). A summary of the results shows is presented at the bottom of the table.

Uncorrected MRI images						Corrected MRI images					
Image Orientation	Level	Dx (mm)	Dy (mm)	Dz (mm)	Dr (mm)	Image Orientation	Level	Dx (mm)	Dy (mm)	Dz (mm)	Dr (mm)
Axial [xy]	1	0.3	0.4	0.48	0.73	Axial [xy]	1	0.29	0.41	0.42	0.7
	2	0.19	0.3	0.4	0.56		2	0.19	0.29	0.36	0.52
	3	0.13	0.19	0.28	0.39		3	0.13	0.19	0.25	0.37
	4	0.13	0.12	0.22	0.31		4	0.14	0.1	0.19	0.29
	5	0.17	0.12	0.19	0.29		5	0.17	0.07	0.17	0.27
	6	0.21	0.12	0.18	0.31		6	0.21	0.07	0.17	0.29
	7	0.24	0.17	0.22	0.4		7	0.24	0.12	0.22	0.36
	8	0.27	0.23	0.29	0.48		8	0.26	0.15	0.28	0.43
	9	0.28	0.3	0.39	0.6		9	0.27	0.22	0.37	0.54
	10	0.29	0.37	0.47	0.69		10	0.29	0.26	0.43	0.61
	11	0.23	0.47	0.59	0.82		11	0.22	0.35	0.55	0.72
	12	0.2	0.55	0.7	0.93		12	0.19	0.38	0.63	0.8
	13	0.19	0.59	0.86	1.07		13	0.19	0.36	0.79	0.92
	14	0.22	0.68	0.91	1.19		14	0.23	0.33	0.84	0.96
Sagittal [yz]	1	0.32	0.31	0.4	0.66	Sagittal [yz]	1	0.32	0.25	0.37	0.6
	2	0.24	0.32	0.4	0.6		2	0.24	0.25	0.36	0.54
	3	0.22	0.32	0.41	0.6		3	0.22	0.23	0.37	0.53
	4	0.2	0.33	0.44	0.62		4	0.2	0.23	0.39	0.54
	5	0.18	0.33	0.45	0.61		5	0.18	0.23	0.41	0.53
	6	0.2	0.32	0.43	0.6		6	0.2	0.22	0.39	0.52
	7	0.22	0.33	0.42	0.61		7	0.22	0.22	0.39	0.53
	8	0.23	0.33	0.45	0.63		8	0.22	0.22	0.42	0.56
Coronal [xz]	1	0.29	0.26	0.36	0.59	Coronal [xz]	1	0.28	0.23	0.32	0.55
	2	0.24	0.28	0.37	0.57		2	0.23	0.25	0.34	0.53
	3	0.21	0.28	0.39	0.56		3	0.2	0.24	0.36	0.52
	4	0.21	0.31	0.39	0.58		4	0.2	0.22	0.36	0.51
	5	0.21	0.33	0.42	0.61		5	0.21	0.23	0.38	0.53
	6	0.21	0.35	0.42	0.62		6	0.21	0.23	0.39	0.54
	7	0.19	0.37	0.42	0.62		7	0.2	0.26	0.39	0.54
	8	0.18	0.36	0.46	0.64		8	0.18	0.24	0.42	0.55
	9	0.19	0.35	0.46	0.64		9	0.18	0.24	0.43	0.55
	10	0.19	0.34	0.47	0.63		10	0.19	0.25	0.43	0.56
	11	0.2	0.37	0.5	0.68		11	0.21	0.26	0.46	0.61
	12	0.24	0.37	0.54	0.72		12	0.25	0.25	0.51	0.65
	13	0.27	0.32	0.52	0.69		13	0.28	0.19	0.47	0.61
Maximum Deviation[mm]		0.32	0.68	0.91	1.19	Maximum Deviation [mm]		0.32	0.41	0.84	0.96
Minimum Deviation [mm]		0.13	0.12	0.18	0.29	Minimum Deviation [mm]		0.13	0.07	0.17	0.27
Mean Absolute Deviation [mm]		0.22	0.33	0.44	0.63	Mean Absolute Deviation [mm]		0.22	0.24	0.4	0.55
Standard Deviation [mm]		0.04	0.12	0.15	0.18	Standard Deviation [mm]		0.04	0.08	0.14	0.15

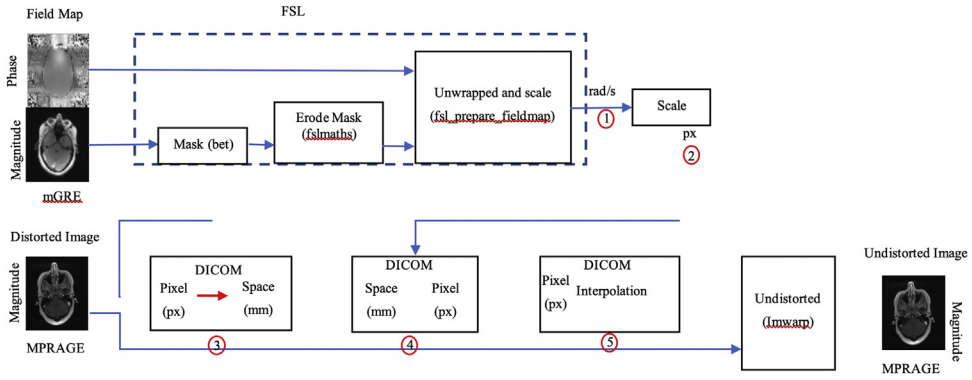

Fig. 3 – Flowchart of the geometrical correction algorithm for MRI images. 1. The field map is generated in FSL (units of rad/s). 2. Field map is converted to a DICOM image in which gray level shows distortion in pixels. 3. The pixels values from MPRAGE are converted to a table coordinate system. 4. The MPRAGE pixels are mapped to pixels of the field map image. 5. Distortion of MPRAGE pixels calculated in field map coordinate system from distortion map in (2).

Table 2 – Representation of maximum and minimum geometrical distortion error (in mm) of MRI images of a CIRS phantom before and after applying our geometrical distortion algorithm. Results were analyzed at different diameters (radius of spherical band) with respect to isocenter of the MRI machine.

Outer radius of spherical band (mm)	20	40	65	70	75	80
Non- Corrected MRI images						
Maximum Error (mm)	0.735	0.751	1.498	0.847	0.787	0.949
Average Error (mm)	0.391	0.311	0.55	0.468	0.517	0.555
Corrected MRI images						
Maximum Error (mm)	0.392	0.723	1.492	0.813	0.774	0.933
Average Error (mm)	0.258	0.331	0.557	0.479	0.528	0.557

the y-direction, 0.07 mm in the z-direction, 0.23 mm in the x-direction and 0.23 mm (absolute distance from the isocenter). For the CIRS head phantom, the corresponding improvements were 0.34 mm, 0.1 mm and 0.09 mm maximum geometrical error correction at diameters of 20, 40 and 60 mm from the isocenter (Table 2). Patient data show a range of correction of 0.2–1.2 mm correction depending on location. The areas of the highest distortion were found around air-cavities, i.e., the sinuses and eyes (Fig. 4).

4. Discussion

MRI-only radiation treatment planning requires images with high geometric stability, clinical relevance, lack of artifacts, ability to be acquired within normal clinical flow, and shorter scanning times.[18,19] In this paper, we proposed a clinical flow to generate distortion-free MRI images for RT planning and compared the results with uncorrected MRI images.

We have previously established a routine QA program to test our magnet for RT planning.[17] We derived the system related distortion map (B_0 inhomogeneity and gradient non-linearity) using commercial phantoms as part of our quality control procedure to monitor system drift over time and applied this information for machine-related geometrical distortion correction. We also used a field map technique for patient-specific geometric distortion correction as a result of magnetic susceptibility changes and chemical shift. The planning sequences are acquired in 3D, as isotropic voxels, using manual shimming along the whole field of view (FOV), and keeping the receiver bandwidth as high as possible while maintaining a reasonably high SNR.

Our approach for patient-specific correction is to use a modified multigradient echo sequence to generate a high-resolution field map in 2 min. This is followed by post-processing to correct MRI images for patient- and machine-specific distortion, and the corrected data are sent back to the MIM software for contouring (another 2 min). This results in a total data processing time of 4 min.

Both phantom and patient data show satisfactory results. We matched field map spatial resolution with T1W-MPRAGE. To accelerate this process in the future, we plan to acquire the field map image simultaneously with planning MRI images. In our recent attempt we used strategically acquired gradient echo (STAGE) imaging for MRI-only stereotactic radiosurgery planning; STAGE takes only 10 min to scan and will generate 8 contrasts, including the field map images.

We tested both commercially available solutions to evaluate geometric distortion of head MR images. Overall, the use of these phantoms is practical and fast, and they can be scanned with a stereotactic radiosurgery G-frame for further investigation. However, they do have some limitations:[20] The GRID^{3D} phantom concentrates on the whole field of view coverage uniformly but does not represent the actual head shape. The CIRS phantom is designed as a head shape phantom but does not mimic tissue or, more importantly, cavities for further evaluation of magnetic susceptibility effects. Neither of the phantoms used has any dosimetric module for RT end-to-end testing.

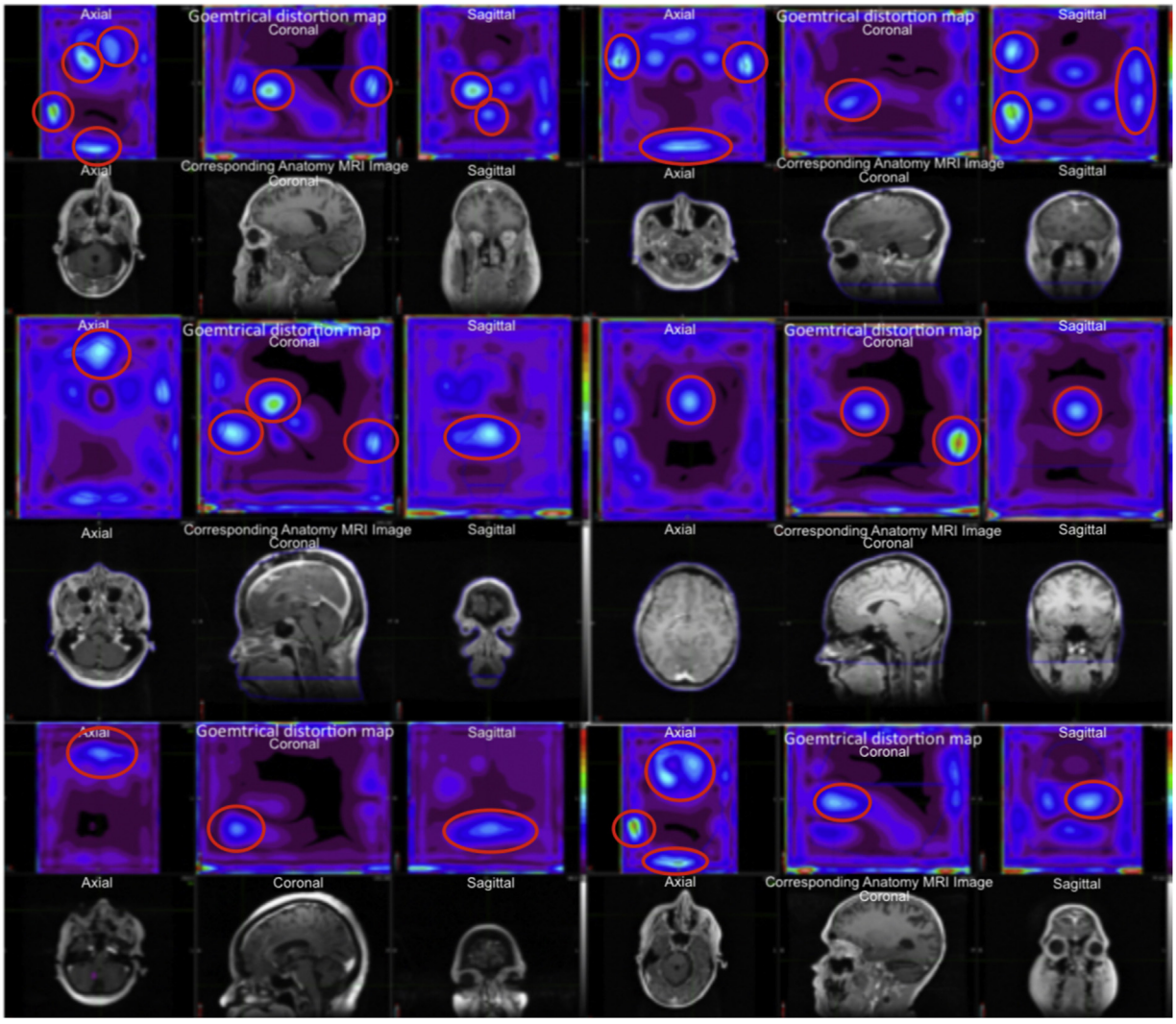

Fig. 4 – Representation of data from six patients. For each patient, the top, raw, images are of the MRI "geometrical distortion map" at three different planes (axial, sagittal and coronal) derived from the difference between corrected and non-corrected MRI images. Images in the bottom row represent the corresponding anatomical region on diagnostic MRI images. The brighter area (inside the red circle) indicates areas of higher degree of distortion. (For interpretation of the references to colour in this figure legend, the reader is referred to the web version of this article).

The data show non-uniform geometrical distortion over the same brain regions among all scanned patients. Therefore, unless some simulation data can predict geometrical distortion over all regions of the brain, we highly recommend caution when referring to and using quantitative data of this type. Most simulation data assume the same human head and tissue composition. Our data show heterogenous results due to changes and variability in human head shape and tissue composition as a result of changes in magnetic susceptibility. In addition, other parameters, such as choosing the right MRI pulse sequences and parameters, the use of localization devices, different field strength MRI machines and accessories, RF coils, co-registration algorithm, and even user expertise, can affect the quality and distortion of the MRI images intended to be used for radiotherapy planning.[21,22]

In general, the maximum distortion was observed close to air cavities such as sinuses and eye globes. One of the limitations of our study is the use of only one sequence for planning. We assume that other sequences can deformably co-register with our corrected images, but in the future we will need to evaluate the accuracy of such co-registration.

Again, geometrical inaccuracies affect the accuracy of MRI based dose delivery[23]; nevertheless, it is only one source of potential errors. Other may be based on the dose calculation methods, that are still usually chosen using CT images. Therefore, for MRI-only based planning, synthetic CT images derived directly from MRI images are a possible solution. Many groups, including our own, are evaluating the geometrical and dosimetric accuracy of synthetic CT images for such MRI-only planning.[24] Our future plan is to use corrected MRI images,

along with synthetic CT and functional quantitative MRI imaging, during the process of RT and post-radiation evaluation.

5. Conclusion

The results of this study indicate the accuracy of our method for patient-specific geometrical distortion correction of MRI images intended for radiotherapy planning. This approach will facilitate the use of MRI-derived information for RT and enhance the collaborative development and sharing of optimized imaging resources between diagnostic radiology and radiotherapy departments in academic and private hospital settings. It will help optimize workflow for patients that may be treated with the evolving next generation of MRI-guided teletherapy systems. Finally, it will directly support the use of emerging MRI-derived biomarkers for individualized adaptive radiotherapy and reduce the cost, as well as the complexity, of longitudinal assessment of treatment outcomes.'

Conflict of interest

None declared.

Financial disclosure

None declared.

Acknowledgements

We would like to thank Siemens Medical for providing us with support.

Appendix A. Supplementary data

Supplementary material related to this article can be found, in the online version, at doi:https://doi.org/10.1016/j.rpor.2019.09.011.

REFERENCES

[1]. Doran SJ, Charles-Edwards L, Reinsberg SA, et al. A complete distortion correction for MR images: I. Gradient warp correction. *Phys Med Biol* 2005;**50**(7):1343, http://dx.doi.org/10.1088/0031-9155/50/7/001.

[2]. Taghizadeh S, Labuda C, Yang CC, et al. Optimizing MRI sequences and images for MRI-based stereotactic radiosurgery treatment planning. *Rep Pract Oncol Radiother J Gt Cancer Cent Poznan Pol Soc Radiat Oncol* 2019;**24**(1):12–9, http://dx.doi.org/10.1016/j.rpor.2018.09.010.

[3]. Weygand J, Fuller CD, Ibbott GS, et al. Spatial precision in magnetic resonance imaging-guided radiation therapy: the role of geometric distortion. *Int J Radiat Oncol Biol Phys* 2016;**95**(4):1304–16, http://dx.doi.org/10.1016/j.ijrobp.2016.02.059.

[4]. Gao Y, Han F, Zhou Z, et al. Distortion-free diffusion MRI using an MRI-guided Tri-Cobalt 60 radiotherapy system: sequence verification and preliminary clinical experience. *Med Phys* 2017;**44**(10):5357–66, http://dx.doi.org/10.1002/mp.12465.

[5]. Torfeh T, Hammoud R, McGarry M, et al. Development and validation of a novel large field of view phantom and a software module for the quality assurance of geometric distortion in magnetic resonance imaging. *Magn Reson Imaging* 2015;**33**(7):939–49, http://dx.doi.org/10.1016/j.mri.2015.04.003.

[6]. Yu C, Petrovich Z, Apuzzo ML, et al. An image fusion study of the geometric accuracy of magnetic resonance imaging with the Leksell stereotactic localization system. *J Appl Clin Med Phys* 2001;**2**(1):42–50, http://dx.doi.org/10.1120/1.1327416.

[7]. Karaiskos P, Moutsatsos A, Pappas E, et al. A simple and efficient methodology to improve geometric accuracy in gamma knife radiation surgery: implementation in multiple brain metastases. *Int J Radiat Oncol Biol Phys* 2014;**90**(5):1234–41, http://dx.doi.org/10.1016/j.ijrobp.2014.08.349.

[8]. Washington CM. *Principles and Practice of Radiation Therapy*. Elsevier Health Sciences; 2015.

[9]. Zhou J, Cao Y, Balter J, et al. Imaging Techniques in Stereotactic Radiosurgery. In: *Principles and Practice of Stereotactic Radiosurgery*. New York, NY: Springer; 2015. p. 11–23.

[10]. Begnozzi L, Benassi M, Bertanelli M, et al. Quality assurance of 3D-CRT: indications and difficulties in their applications. *Crit Rev Oncol Hematol* 2009;**70**(1):24–38, http://dx.doi.org/10.1016/j.critrevonc.2008.07.016.

[11]. Pappas EP, Alshanqity M, Moutsatsos A, et al. MRI-related geometric distortions in stereotactic radiotherapy treatment planning: evaluation and dosimetric impact. *Technol Cancer Res Treat* 2017;**16**(6):1120–9, http://dx.doi.org/10.1177/1533034617735454.

[12]. Van Herk M. Will IGRT live up to its promise? *Acta Oncol Stockh Swed* 2008;**47**(7):1186–7, http://dx.doi.org/10.1080/02841860802279717.

[13]. Tai P, Van Dyk J, Battista J, et al. Improving the consistency in cervical esophageal target volume definition by special training. *Int J Radiat Oncol Biol Phys* 2002;**53**(3):766–74.

[14]. van der Put RW, Raaymakers BW, Kerkhof EM, et al. A novel method for comparing 3D target volume delineations in radiotherapy. *Phys Med Biol* 2008;**53**(8):2149–59, http://dx.doi.org/10.1088/0031-9155/53/8/010.

[15]. Narayanasamy G, Stathakis S, Gutierrez AN, et al. A systematic analysis of 2 monoisocentric techniques for the treatment of multiple brain metastases. *Technol Cancer Res Treat* 2017;**16**(5):639–44, http://dx.doi.org/10.1177/1533034616666998.

[16]. Fatemi A, Taghizadeh S, Yang CC, et al. Machine-specific magnetic resonance imaging quality control procedures for stereotactic radiosurgery treatment planning. *Cureus* 2017;**9**(12):e1957, http://dx.doi.org/10.7759/cureus.1957.

[17]. aldwin LN, Wachowicz K, Fallone BG. A two-step scheme for distortion rectification of magnetic resonance images. *Med Phys* 2009;**36**(9):3917–26, http://dx.doi.org/10.1118/1.3180107.

[18]. Schakel T, Hoogduin JM, Terhaard CHJ, et al. Technical note: diffusion-weighted MRI with minimal distortion in head-and-neck radiotherapy using a turbo spin echo acquisition method. *Med Phys* 2017;**44**(8):4188–93, http://dx.doi.org/10.1002/mp.12363.

[19]. Lau JC, Khan AR, Zeng TY, et al. Quantification of local geometric distortion in structural magnetic resonance images: application to ultra-high fields. *NeuroImage* 2018;**168**:141–51, http://dx.doi.org/10.1016/j.neuroimage.2016.12.066.

[20]. Damyanovich AZ, Rieker M, Zhang B, et al. Design and implementation of a 3D-MR/CT geometric image distortion phantom/analysis system for stereotactic radiosurgery. *Phys Med Biol* 2018;**63**(7):075010, http://dx.doi.org/10.1088/1361-6560/aab33e.

[21]. Piotrowski T, Kaczmarek K, Bajon T, Ryczkowski A, Jodda A, Kaźmierska J. Evaluation of image-guidance strategies for prostate cancer. *Technol Cancer Res Treat* 2014;**13**(6):583–91, http://dx.doi.org/10.7785/tcrtexpress.2013.600258.

[22]. Adamczyk M, Piotrowski T, Adamiak E, Malicki J. Dosimetric consequences of prostate-based couch shifts on the precision of dose delivery during simultaneous IMRT irradiation of the prostate, seminal vesicles and pelvic lymph nodes. *Phys Medica PM Int J Devoted Appl Phys Med Biol Off J Ital Assoc Biomed Phys AIFB* 2014;**30**(2):228–33, http://dx.doi.org/10.1016/j.ejmp.2013.06.003.

[23]. Yan Y, Yang J, Beddar S, et al. A methodology to investigate the impact of image distortions on the radiation dose when using magnetic resonance images for planning. *Phys Med Biol* 2018;**63**(8):085005, http://dx.doi.org/10.1088/1361-6560/aab5c3.

[24]. Fatemi Ali, Kanakamedala MR, Yang CC, Morris B, Duggar WN, Vijayakumar S. Evaluation of the geometric and dosimetric accuracy of synthetic computed tomography images for magnetic resonance imaging-only stereotactic radiosurgery. *Cureus* 2019, http://dx.doi.org/10.7759/cureus.4404.